

## Mechanisms for phase distortion in a traveling wave tube

John G. Wöhlbier\* and John H. Booske

Department of Electrical and Computer Engineering, University of Wisconsin, Madison, Wisconsin 53706, USA

(Received 14 August 2003; revised manuscript received 23 December 2003; published 4 June 2004)

We present a view of the physics of phase distortion in a traveling wave tube (TWT) based on unique insights afforded by the MUSE models of a TWT [J. Wöhlbier, J. Booske, and I. Dobson, *IEEE Trans. Plasma Sci.* **30**, 1063 (2002)]. The conclusion, supported by analytic theory and simulations, is that prior to gain compression phase distortion is due to harmonic frequencies in the electron beam and the resulting “intermodulation” frequency at the fundamental, and not the often cited “slowing down of electrons in the electron beam.” We draw these conclusions based on MUSE simulations that allow explicit control of electron beam frequency content, an analytic solution to the S-MUSE model [J. Wöhlbier, J. Booske, and I. Dobson, *IEEE Trans. Plasma Sci.* **30**, 1063 (2002)] that reveals that phase distortion is due to the fact that the fundamental frequency is an intermodulation product of itself, and large signal LATTE [J. Wöhlbier, J. Booske, and I. Dobson, *IEEE Trans. Plasma Sci.* **30**, 1063 (2002)] simulations that are modified to remove the effect of the slowing down of electrons in the electron beam. As applications of the theory we compare S-MUSE simulations to an amplitude phase model using the analytic phase transfer curve, we study dependence of phase distortion on circuit dispersion and electron beam parameters at the second harmonic with large signal LATTE simulations for narrow and wide band TWT designs, and we consider the phase distortion theory in the context of TWT linearization.

DOI: 10.1103/PhysRevE.69.066502

PACS number(s): 52.59.Rz, 84.40.Fe, 84.47.+w, 52.35.Mw

### I. INTRODUCTION

Traveling wave tubes (TWTs) are widely used as amplifiers in communications and electronic countermeasure systems. It is well known that in many applications amplifier nonlinearities can compromise system performance. This paper is part of a continuing effort to understand sources of nonlinear distortions in TWTs using simulation and analysis.

Conventionally, TWT nonlinearity has been quantified via single frequency input-output transfer characteristics. In particular AM/AM (output power vs input power) curves and AM/PM (the derivative of output phase vs input power) curves are used (see Fig. 1). AM/AM curves exhibit a “linear gain” region, followed by “nonlinear” gain compression and saturation for increasing input powers. In a linear amplifier the AM/PM curve is a flat line, i.e., the difference in phase between the output and the input does not depend on input power. In the TWT, as with any amplifier, the output phase does depend on input power as seen in Fig. 1. The physics of this dependence is the subject of this paper. One sees in Fig. 1 that the AM/PM curve deviates from linear behavior for input powers much smaller than those that first produce compression in the AM/AM curve. This shows that phase distortion in TWTs is significant even in the regime defined as the linear gain region based on the AM/AM characteristics.

From a systems perspective the AM/AM and AM/PM nonlinearities are said to “cause” undesirable output spectral content such as intermodulation products [1]. However, since the transfer curves come from a single frequency input-output measurement, they do not contain explicit information about the physics internal to the TWT. In fact, from a physics

perspective it is better to say that the transfer curves “capture” aspects of TWT nonlinearity, and thus can be used to predict input-output behavior of the TWT. For example, an input-output model such as an *amplitude-phase model* [2] using the single frequency TWT transfer characteristics predicts intermodulation spectrum around closely spaced carriers [3], but the amplitude-phase model does not predict harmonics of the carrier frequencies. Since it is well established that the carrier harmonics (and sum frequencies) exist in the output spectrum of a TWT, one concludes that the single frequency transfer characteristics capture certain nonlinear

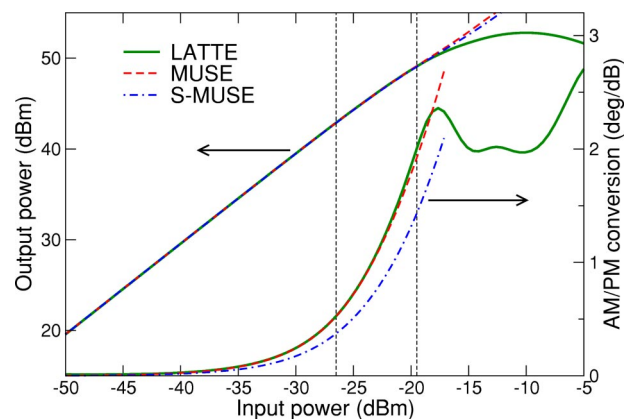


FIG. 1. AM/AM and AM/PM curves at 14 GHz generated by LATTE, MUSE, and S-MUSE for the TWT parameters in Tables I and II. The vertical lines at  $P_{in} = -19.5$  dBm and  $P_{in} = -26.5$  dBm correspond to 1 dB gain compression (3.8 dB backed off from saturation) and 10 dB backed off from saturation, respectively, as predicted by LATTE. The simulations to generate the results accounted for circuit frequencies up to the third harmonic and ten space charge harmonics.

\*Present address: LANL, MS H851, Los Alamos, NM 87545.

physics of the TWT, but fail to capture other nonlinear physics.

The physics behind the AM/AM curve can be understood in terms of power saturation, which is a result of electron bunches falling into accelerating phases of the rf wave and hence taking energy from the rf wave. The physics of phase nonlinearity, we claim, is less well understood. Several authors have claimed that phase distortion is due to the reduction of the average electron beam velocity. For example, Gilmour [4] claims that phase distortion “occurs because, as drive level is increased, more power is extracted from the electron beam and the velocity of the beam is reduced. As beam velocity decreases, the velocity of the rf wave on the circuit is reduced and this increases the phase length of the TWT.” Furthermore, Ezura and Kano [5] state “in Refs. [1–5] where saturation was excluded, one may easily grasp the physical image of the phase distortion due to the decrease of the electron velocities, but not quantitatively.” However, in this paper we show using several arguments that, at least prior to 1 dB of gain compression, the slowing down of the electron beam is not the dominant mechanism for phase distortion.

Dimonte and Malmberg studied TWT phase distortion in the context of trapping oscillations [6], i.e., in operating regimes where the TWT is strongly overdriven. Although this is an interesting regime to understand physics, in a practical amplifier there are “no compelling reasons to study the interaction much beyond saturation” [6]. The explanation of phase distortion in Ref. [6] relies on energy conservation relations of approximate single frequency models. Ultimately the phase evolution simply appears as a term in a conservation relation that must shift to “simultaneously balance energy flow.” [6] In contrast to the motivation of Ref. [6] which was the nonlinear physics beyond saturation, our model development emphasizes the physics of phase distortion prior to saturation, and we provide a functional, quantitative predictive model of phase distortion.

In this paper we offer a view of phase distortion provided by the new spectral TWT models MUSE and S-MUSE [7]. By artificially suppressing harmonic and dc effects in the electron beam equations of the MUSE model, we show that the beam second harmonic plays a far greater role in the AM/PM distortion prior to gain compression and power saturation than the average slowing down of electrons. Next, using an approximate analytic solution of the output phase for the approximate nonlinear model S-MUSE, we conclude that the phase distortion prior to gain compression is mostly a result of the fact that the fundamental frequency is an intermodulation frequency of itself. We also compare the spectrum of an amplitude-phase model using the output phase of the approximate analytic solution to the spectrum predicted by simulation of the S-MUSE model. Furthermore, since it is found that phase distortion depends primarily on the second harmonic existing in the electron beam, we study the dependence of the phase distortion on circuit dispersion and electron beam parameters at the second harmonic. Finally, using insights developed throughout the paper we discuss our phase distortion theory in the context of TWT linearization.

In Sec. II we give an overview of the TWT models used in our study, referring the reader to Ref. [7] for model details.

In Sec. III we present simulation, theory, and physical arguments to support the case that the majority of phase distortion, at least prior to 1 dB of gain compression, is due to beam harmonics and intermodulation distortion of the fundamental with itself, and not due to the slowing down of electrons in the beam. In Sec. IV we compare S-MUSE simulations of two frequency inputs to results from an amplitude-phase model that uses the output phase of the approximate analytic solution of the S-MUSE model. Section V presents results from parametric studies of phase distortion as a function of circuit dispersion and beam parameters at the second harmonic. We discuss TWT linearization in Sec. VI, and the paper is concluded in Sec. VII. Two appendixes provide theoretical detail to support Sec. III.

## II. TWT MODELS

In this paper we use the nonlinear TWT models MUSE, S-MUSE, and LATTE derived in Refs. [7,8]. MUSE and LATTE are frequency domain formulations of the same initial equations where MUSE uses Eulerian coordinates for the electron beam and LATTE uses Lagrangian coordinates for the electron beam. The S-MUSE model is obtained from MUSE by neglecting certain nonlinearities, and was derived because it is analytically solvable while retaining many salient nonlinear features of MUSE. The major implication of choosing Eulerian coordinates in MUSE and S-MUSE is that, unless special methods are employed [9], the models do not predict electron overtaking and hence do not agree with Lagrangian models in the region of power saturation. However, there is much physics to be learned from the Eulerian models prior to electron overtaking as this and other work [10–12] have shown. The reader is referred to Ref. [7] for detailed analysis and comparison of the models.

For the present work there are two primary benefits of the Eulerian models over Lagrangian models such as LATTE. First, the spectral representation of the electron beam in MUSE allows one to investigate how electron beam frequencies, including “dc” effects such as the reduction of the average electron beam velocity, affect phase distortion. In principle, Lagrangian simulations may also be modified to eliminate spectral components from the electron beam description by generalizing a method we present in this paper. However, such modifications are far more cumbersome than the analogous MUSE simulations. Second, S-MUSE possesses an analytic solution which has a direct physical interpretation of phase distortion not afforded by either MUSE or LATTE.

The TWT models in Ref. [7] are derived from a one-dimensional (1D) nonlinear model which uses transmission line equations to represent the slow wave circuit and Eulerian electron beam equations. The MUSE model is the result of a spectral analysis of these equations, whereas LATTE is the result of spectral analysis of the field quantities and a transformation of the electron beam equations to Lagrangian coordinates. Both models are steady state and assume that all frequencies present are integer multiples of a base frequency  $\omega_0$ . There are five quantities in the TWT description: transmission line voltage  $V$ , transmission line current  $I$ , space

charge electric field  $E$ , electron beam velocity  $v$ , and electron beam charge density  $\rho$ . The MUSE model is a system of ordinary differential equations for the spatially dependent complex Fourier coefficients of the five quantities per frequency:  $\tilde{V}_\ell(z), \tilde{I}_\ell(z), \tilde{E}_\ell(z), \tilde{v}_\ell(z)$ , and  $\tilde{\rho}_\ell(z)$  where  $\ell$  indexes the frequency  $f_\ell \omega_0$  and  $z$  is the axial distance. From the Fourier coefficients the circuit voltage may be synthesized via

$$V(z, t) = \sum_{\ell=-\infty}^{\infty} \tilde{V}_\ell(z) e^{if_\ell \omega_0 ([z/u_0] - t)}, \quad (1)$$

where  $u_0$  is the dc electron beam velocity. The other physical variables may be similarly synthesized from their Fourier coefficients.

For the circuit quantities and space charge field LATTE retains  $\tilde{V}_\ell(z), \tilde{I}_\ell(z)$ , and  $\tilde{E}_\ell(z)$ . However, the Eulerian electron beam velocity and density functions  $v^E(z, \psi)$  and  $\rho^E(z, \psi)$  are transformed to the Lagrangian velocity and density functions  $v^L(z, \psi_0)$  and  $\rho^L(z, \psi_0)$ . We also define the function  $\Psi(z, \psi_0)$  which is the nonlinear transformation between the coordinate systems and represents the phase position of fluid element  $\psi_0$  with respect to the stream wave [13] at axial position  $z$ . See Ref. [7] for details of the transformation between Eulerian and Lagrangian coordinates.

### III. PHASE DISTORTION MECHANISMS

In this section we study using simulation and analysis the mechanisms of phase distortion. We define  $\Phi(P_{\text{in}})$  as the phase difference between the TWT output and input of the “hot” circuit voltage wave at frequency  $f_\ell \omega_0$ , where the “small signal” phase difference is subtracted off. Using this definition, any nonzero value of  $\Phi$  is considered a “distortion” from the linear behavior. The term hot refers to the fact that the spatially dependent local velocity and local wave number of the voltage wave at frequency  $f_\ell \omega_0$  are in general not equal to the “cold circuit” quantities, i.e., the velocity and wave number of a voltage wave with no beam present, nor are they in general equal to the electron beam velocity  $u_0$  or effective electron stream wave number  $f_\ell \omega_0 / u_0$ . Rather, the local velocity and wave number of the hot wave must be computed from analytic theory or simulation.

If we define  $\beta_{\text{lin}}$  as the hot wave number predicted by linear theory [14], i.e., the wave number corresponding to the exponentially growing mode of the solution, and  $\beta_{\text{nl}}(P_{\text{in}}, z)$  as a local hot wave number predicted by either nonlinear analytic theory or nonlinear simulation, then we have

$$\Phi(P_{\text{in}}) = \int_0^L [\beta_{\text{nl}}(P_{\text{in}}, z) - \beta_{\text{lin}}] dz, \quad (2)$$

where  $z=L$  is the TWT output. Note that  $\beta_{\text{lin}}$  is independent of input power  $P_{\text{in}}$  and axial position  $z$ . For small input powers  $\beta_{\text{nl}}$  tends to  $\beta_{\text{lin}}$ .

Rewriting Eq. (2) in terms of linear and nonlinear hot phase velocities  $v_{\text{lin}}^{\text{hot}}$  and  $v_{\text{nl}}^{\text{hot}}(P_{\text{in}}, z)$  we get

TABLE I. Ku-band TWT electron beam and circuit parameters.

Parameter	Value
Cathode voltage	-4.92 kV
Beam current	0.177 A
Beam radius	0.3175 mm
Helix radius	0.60 mm

$$\Phi(P_{\text{in}}) = f_\ell \omega_0 \int_0^L \left[ \frac{1}{v_{\text{nl}}^{\text{hot}}(P_{\text{in}}, z)} - \frac{1}{v_{\text{lin}}^{\text{hot}}} \right] dz. \quad (3)$$

Therefore, by definition phase distortion is the result of the nonlinear velocity change of the hot circuit wave. When the cold circuit velocity is less than the dc electron beam velocity (Pierce velocity parameter  $b > 0$ ), the hot velocity usually first slows down relative to  $v_{\text{lin}}^{\text{hot}}$ , increasing the electrical length of the TWT relative to the linear behavior, and can speed back up in saturation. When the cold circuit velocity is greater than the dc electron beam velocity (Pierce velocity parameter  $b < 0$ ), the hot velocity usually first speeds up relative to  $v_{\text{lin}}^{\text{hot}}$ , decreasing the electrical length of the TWT relative to the linear behavior, and can slow back down in saturation (see, for example, Fig. 1 of Ref. [5]). In general the factors influencing  $v_{\text{nl}}^{\text{hot}}(P_{\text{in}}, z)$  are not fully understood for all operating regimes of the TWT.

It will be useful to define hot phase velocity using the model variables we have introduced. For frequency  $f_\ell \omega_0$  we write a term of Eq. (1) as

$$|\tilde{V}_\ell(z)| e^{i\theta_\ell(z)} e^{if_\ell \omega_0 ([z/u_0] - t)}, \quad (4)$$

and from this one can find that

$$v_\ell^{\text{hot}}(z) = \frac{f_\ell \omega_0}{\beta_\ell + \frac{d\theta_\ell}{dz}}, \quad (5)$$

where  $\beta_\ell = f_\ell \omega_0 / u_0$  is the stream wave number.

#### A. Simulation results

For the first set of simulation studies we choose parameters for a representative Ku-band TWT. The electron beam and circuit parameters are listed in Table I and the cold circuit phase velocity  $\tilde{v}_{\text{ph}}$ , interaction impedance  $\tilde{K}$ , and space charge reduction factor  $\tilde{R}$  [4,14] are found in Table II. The parameters represent a single lossless, constant pitch section. AM/AM and AM/PM curves at 14 GHz are given in Fig. 1.

TABLE II. Ku-band TWT dispersion parameters.

$f$ (GHz)	$\tilde{v}_{\text{ph}} (\times 10^7 \text{ m/s})$	$\tilde{K} (\Omega)$	$\tilde{R}$
14.0	3.858	32.625	0.156
28.0	3.673	1.161	0.389
42.0	3.591	0.061	0.547

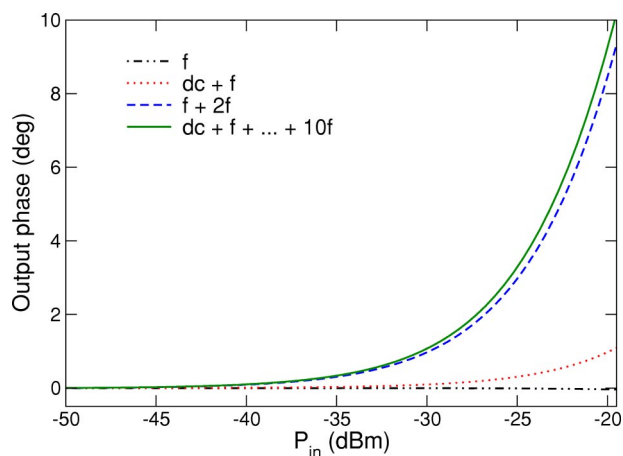


FIG. 2. Output phase vs input power curves generated by MUSE simulations with varying frequencies included in the simulation. The legend indicates which frequencies were included in the simulation generating the trace. The maximum input power represented on the graph corresponds to the 1 dB gain compression point as seen in Fig. 1. For the input powers in this figure LATTE and MUSE have nearly identical phase predictions accounting for dc through the tenth harmonic, as seen in Fig. 1.

Space charge reduction factors for harmonics higher than the third are computed by Eq. (23b) of Ref. [15].

Since the Eulerian models apply only prior to electron overtaking, we restrict our attention in this section to input powers smaller than the 1 dB gain compression point. From the AM/AM curve in Fig. 1 we find that for our TWT design this corresponds to 3.8 dB backed off from saturation. According to Ref. [4] the maximum point of AM/PM distortion typically occurs anywhere between 3 and 10 dB backed off from saturation, indicating that the input powers to which we restrict our attention are of practical interest.

The spectral structure of the MUSE model allows one to artificially suppress electron beam (and circuit) frequencies as a diagnostic tool to discover where various nonlinearities manifest in TWT behavior. In the following MUSE simulations we include and exclude dc effects [time average electron beam velocity  $\bar{v}_0(z)$  and time average electron beam charge density  $\bar{\rho}_0(z)$ ], second harmonics, and higher order harmonics. A frequency  $f_\ell\omega_0$  is excluded from a simulation by forcing derivatives of the TWT state variables at that frequency (e.g.,  $d\bar{v}_\ell/dz, d\bar{\rho}_\ell/dz$ , etc.) to zero in the simulation.

Figure 2 shows output phase versus input power curves from MUSE simulations with varying frequencies included. When the fundamental frequency ( $f$ ) is the only frequency in the simulation the model reduces to a linear model, and there is no phase distortion. Separately including the dc frequency and the second harmonic with the fundamental alone (“dc +  $f$ ” and “ $f + 2f$ ,” respectively) indicates that most of the phase distortion is associated with the inclusion of the second harmonic and not due to reduction of the dc velocity of the beam. Furthermore, including all frequencies up to the tenth harmonic (dc +  $f + \dots + 10f$ ) supports the conclusion that most of the phase distortion is associated with the inclusion of the second harmonic. When the second harmonic is

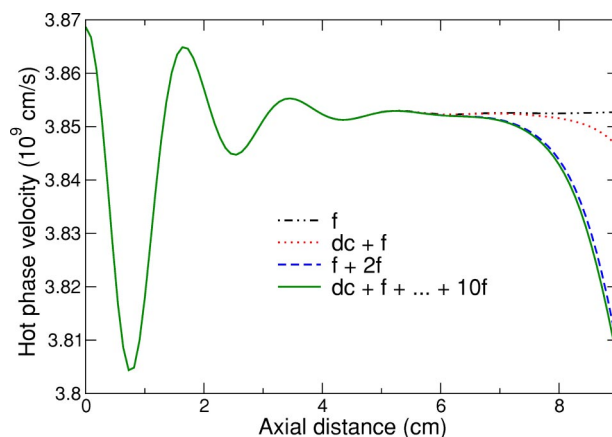


FIG. 3. MUSE computations of the hot phase velocity, Eq. (5), at the fundamental frequency with varying frequencies included in the simulation. The legend indicates which frequencies were included in the simulation generating the trace. The input power  $P_{in} = -19.5$  dBm corresponds to the 1 dB gain compression point shown in Fig. 1. For this input power the phase difference as predicted by LATTE is nearly identical to MUSE when accounting for dc through the tenth harmonic.

added to the simulation ( $f + 2f$ ) we include both the circuit and beam second harmonic components. Therefore, the relative influence of the beam second harmonic vs the circuit second harmonic on the level of phase distortion cannot be gleaned from Fig. 2.

Since the circuit voltage hot phase velocity is the physical quantity internal to the TWT that causes phase distortion [see Eq. (3)], we look at MUSE predictions of hot phase velocity for  $P_{in} = -19.5$  dBm including and excluding different frequencies. The results shown in Fig. 3 confirm that the inclusion of the second harmonic accounts for most of the change in hot phase velocity, which in turn accounts for most of the phase distortion in Fig. 2 via Eq. (3). The variation of the hot phase velocity for  $z \leq 4$  cm is due to the mixing of the three modes of linear Pierce theory [14].

To get a feel for the level of the circuit and beam harmonic distortions in the case of Fig. 3, we plot in Fig. 4 the circuit power at the fundamental through third harmonic, and the magnitude of the beam density modulation at the fundamental through tenth harmonics. Note that at the output ( $z = 9$  cm) the second harmonic circuit power is about 20 dB less than the fundamental, while all of the beam charge density modulation harmonics are within 1 dB of each other. This indicates that even in a narrow band TWT, where the second harmonic is out of the linear gain bandwidth, the harmonic beam modulations are very strong, even at an input power corresponding to the 1 dB gain compression point. The beam velocity harmonics, not shown here, look very similar to the beam charge density harmonics, and are within 1.3 dB of each other at the output.

Next we provide more evidence that the average velocity reduction in the electron beam is not the primary cause of phase distortion by using MUSE and LATTE simulations as well as a physical argument. First we consider a large signal LATTE simulation that has been modified to remove the average velocity reduction using the approach given in Appen-

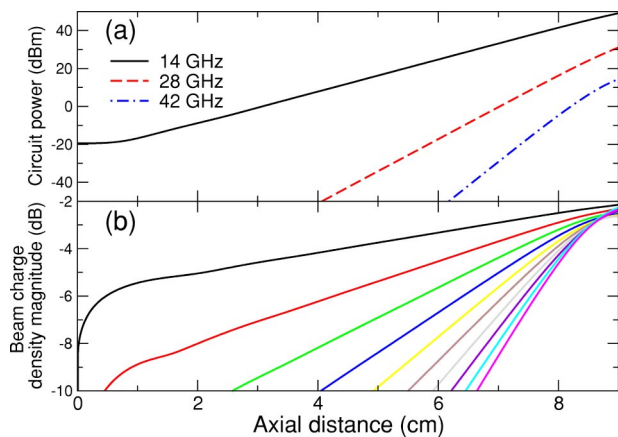


FIG. 4. Circuit power at the fundamental through third harmonic (a), and beam charge density magnitude at the fundamental through tenth harmonic (b) for the case of Fig. 3. For  $z \leq 8$  cm in (b), the charge density magnitude at the fundamental frequency is the largest and the magnitudes of the higher order harmonics decrease with increasing harmonic order. At the output ( $z=9$  cm) the second harmonic circuit power is about 20 dB less than the fundamental, while all of the beam charge density modulation harmonics are within 1 dB of each other.

dx B. In Fig. 5 we show the phase distortion produced by LATTE simulations with and without the average velocity adjustment. The result confirms that average velocity reduction, at least prior to gain compression, is not the primary cause of the phase distortion.

We limit the maximum power in Fig. 5 to  $P_{in} = -23$  dBm for computational reasons. As discussed in Appendix B, we use Eq. (B6) to compute the evolution of the average disk velocity in a LATTE simulation. For input powers greater than or equal to  $P_{in} = -23$  dBm, the number of space charge harmonics required for Eq. (B6) to converge can become quite large. For convergence with  $P_{in} = -23$  dBm 100 space charge harmonics were required.

To verify that the average velocity computed from the Lagrangian calculation of Eq. (B6) agrees with the MUSE

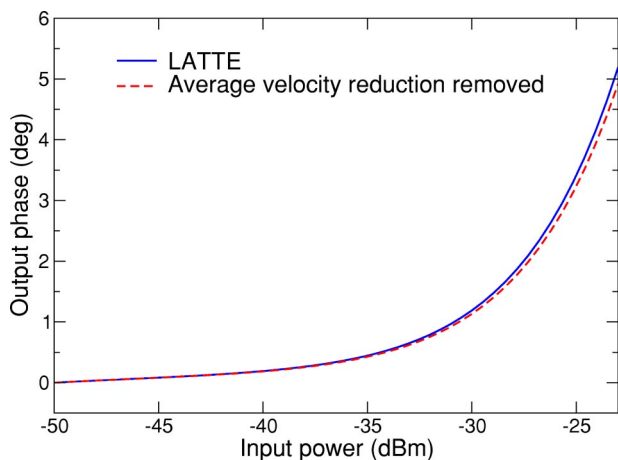


FIG. 5. Output phase for LATTE simulations with and without removal of the average beam velocity reduction as described in Appendix B. One hundred space charge harmonics were used to compute  $\langle v \rangle_0$  from Eq. (B6).

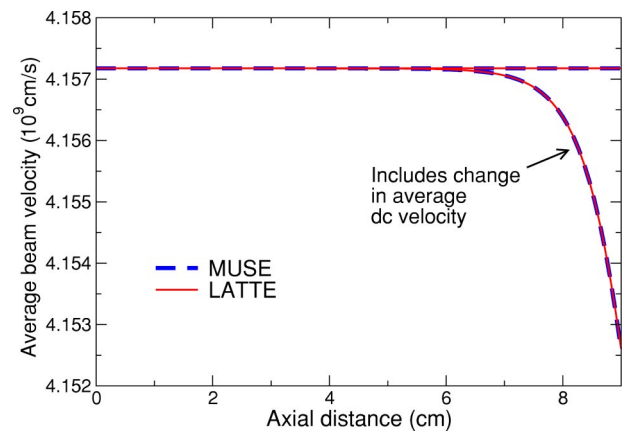


FIG. 6. Average electron beam velocities computed by LATTE and MUSE. LATTE traces were computed by Eq. (B6), MUSE traces are the dc frequency of the velocity  $\tilde{v}_0(z)$ . Shown are computations with and without the velocity adjusted to remove the change in the dc component. The input power used to generate the traces is  $P_{in} = -23$  dBm, which is the maximum power appearing in Fig. 5.

computation of the dc component of the beam velocity  $\tilde{v}_0(z)$ , we compare the average beam velocities of both models before and after the removal of the spatially evolving average velocity for  $P_{in} = -23$  dBm in Fig. 6. For this input power note that the average electron beam velocities predicted by MUSE and LATTE are virtually identical.

Finally, we consider how the reduction of the average beam velocity could not account for the majority of phase distortion. First we consider a comparison of the hot phase velocity predicted by MUSE and LATTE [computed using Eq. (5)] to the average beam velocity computed by MUSE in Fig. 7 for  $P_{in} = -20$  dBm. According to Fig. 2, the phase distortion for this input power is about  $10^\circ$  which, according to Fig. 7, corresponds to a change in hot phase velocity of about 1%. As seen in Fig. 7 the average beam velocity for this input power only reduces from its initial value by 0.2%. If this reduction in beam velocity solely determined the change in the hot phase velocity to cause phase distortion, then over the length of 0.5 cm [16] Eq. (3) indicates that this only

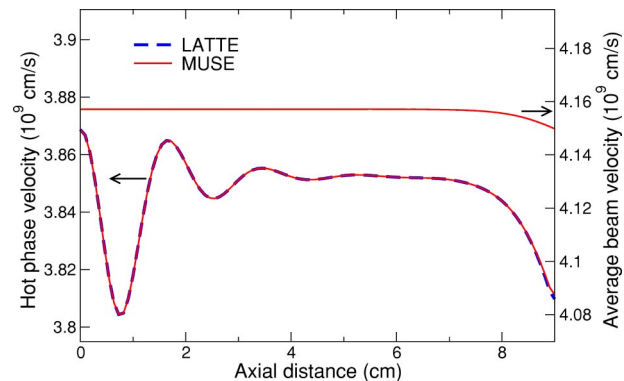


FIG. 7. Average electron beam velocity computed by MUSE, and hot phase velocity at the fundamental computed by LATTE and MUSE for  $P_{in} = -20$  dBm. The ranges of values on both vertical axes are 3% of the value of the respective curve at  $z=5$  cm.

accounts for about  $1.3^\circ$  of phase distortion, far below the  $10^\circ$  seen in Fig. 2.

### B. Analytic results

The Eulerian model S-MUSE [7], a simplification of MUSE, admits an analytic solution which allows us to probe further into the physical mechanisms of phase distortion. Because of the approximations made in deriving the S-MUSE model, the phase distortion predicted by MUSE, S-MUSE, and LATTE agree qualitatively but not quantitatively. However, we postulate that the physical interpretations made for the S-MUSE model are also true for the MUSE and LATTE models for input powers prior to gain compression.

The structure of the S-MUSE solution for a physical variable at a particular frequency is a linear combination of  $z$  dependent complex exponentials [10–12]. For example, the voltage at the fundamental may be approximated as

$$\begin{aligned} \tilde{V}_1(z, t) = & \{A_{\text{dr}} \exp(\mu_{\text{dr}} + i\kappa_{\text{dr}})z + \sum_q A_{\text{nl}}^q \exp(\mu_{\text{nl}}^q \\ & + i\kappa_{\text{nl}}^q)z\} e^{if_1\omega_0([z/u_0]-t)}, \end{aligned} \quad (6)$$

where the dr subscript refers to the driven portion of the solution, i.e., the exponentially growing mode due to the fundamental input, and the nl subscript refers to quantities occurring as a result of the nonlinear interactions. The subscript 1 appearing in  $\tilde{V}_1$  and  $f_1$  refer to the fundamental frequency. In Eq. (6)  $A_{\text{dr}}$ ,  $A_{\text{nl}}^q$  are complex and  $\mu_{\text{dr}}$ ,  $\mu_{\text{nl}}^q$ ,  $\kappa_{\text{dr}}$ ,  $\kappa_{\text{nl}}^q$  are real. Forms similar to Eq. (6) apply to the other TWT state variables at the fundamental frequency.

In Eq. (6) each complex exponential is related to a particular order of intermodulation product [17], and each successive term in the sum over  $q$  accounts for the next higher order odd intermodulation product (third, fifth, etc.). Since the fundamental frequency is an odd order intermodulation product of itself, e.g.,  $2f_1 - f_1 = 3f_1 - 2f_1 = f_1$  etc., we can approximate Eq. (6) as

$$\tilde{V}_1(z, t) = \{A_{\text{dr}} e^{\gamma_{\text{dr}} z} + A_{\text{nl}}^{3\text{IM}} e^{\gamma_{\text{nl}}^{3\text{IM}} z} + A_{\text{nl}}^{5\text{IM}} e^{\gamma_{\text{nl}}^{5\text{IM}} z} + \dots\} e^{if_1\omega_0([z/u_0]-t)}, \quad (7)$$

where we have written the growth rates  $\mu$  and wave numbers  $\kappa$  in Eq. (6) together as complex propagation constants  $\gamma$ .

The complete solution to S-MUSE is made up of an infinite number of complex exponentials [11,12]. In Eq. (7) we only express the dominant terms and ignore the terms that do not contribute appreciably to the solution near the output of the TWT. Due to the neglect of nongrowing or weakly growing modes in Eqs. (6) and (7), both from the linear and nonlinear portions of the solution, evaluation of the equations at  $z=0$  does not give the correct value of the input. The equations are therefore only good approximations, both in amplitude and phase, for lengths such that the exponentially growing modes dominate the total solution (for example  $z \geq 4$  cm in Fig. 7). In Appendix A we provide the details of the analytic solution of S-MUSE required to compute Eqs. (6) and (7).

In Fig. 8 we compare the output phase computed with Eq. (6) to the output phase obtained by numerical solution of the

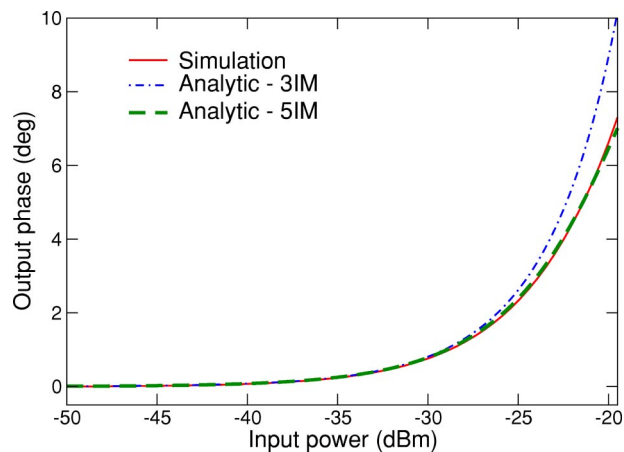


FIG. 8. Numerical solutions and analytic predictions of S-MUSE output phase. For the phase of Eq. (7) to match the numerical solution the contributions from 3IM and 5IM terms need to be included. The maximum input power represented on the graph corresponds to the 1 dB gain compression point as seen in Fig. 1. The numerical solution accounts for circuit frequencies up to the third harmonic and ten space charge harmonics.

S-MUSE equations (Eqs. (25)–(29) of Ref. [7]) for input powers up to the 1 dB compression point. We show the output phase of Eq. (6) accounting for only the 3IM and also accounting for the 3IM and the 5IM. The analytic prediction accounting for the 5IM matches the simulation almost identically.

Comparing the AM/PM curves (derivatives of the output phase) of S-MUSE and LATTE in Fig. 1 we see that S-MUSE predicts most of the phase distortion of the large signal simulation prior to gain compression. Then from Fig. 8 we conclude that the majority of the *large signal* TWT phase distortion [18] prior to gain compression is predicted by Eq. (6). Hence the primary mechanism for the large signal phase distortion is that the fundamental frequency is an intermodulation product of itself, which is the view that comes from the analytic solution to the S-MUSE model. We attribute the output phase discrepancies between LATTE and S-MUSE to the nonlinearities that were neglected in deriving S-MUSE, including the approximation of the average beam velocity and the average charge density as constants, and the resulting underpredictions of intermodulation spectra by S-MUSE as can be seen in Ref. [7].

Based on the above comparison of large signal simulations to the analytic solution to S-MUSE, and supported by the simulations of Sec. III A, we submit the following view of TWT phase distortion valid prior to gain compression, and speculatively into saturation.

The fundamental drive frequency induces second harmonic distortions on the electron beam, and hence into second harmonic circuit quantities. These second harmonic distortions combine back with the beam and circuit quantities at the fundamental frequency to produce distortions in the beam quantities, and hence the circuit voltage, at the fundamental frequency. In a similar manner the third harmonic distortions in the electron beam and circuit combine with the second harmonic beam and circuit distortions to produce dis-

tortions in the circuit voltage at the fundamental frequency.

This process also occurs for higher order harmonics, but to a more limited extent as the order becomes higher. Therefore, the voltage at the fundamental frequency is composed of the driven mode, the 3IM and 5IM distortion modes, as well as higher order odd intermodulation modes. The relative weights of the driven mode and the distortion modes determine the evolving phase of the fundamental circuit voltage, and hence the evolving hot phase velocity of the fundamental circuit voltage. The hot phase velocity then determines the phase distortion via Eq. (3). The S-MUSE equations (Eqs. (25)–(29) of Ref. [7]) may be used to convince oneself of the above mixing process.

One may wonder why in Fig. 2 the  $f+2f$  MUSE simulation produced an output phase smaller than the  $f+\dots+10f$  MUSE simulation, while in Fig. 8 the S-MUSE analytic solution accounting only for the 3IM mode predicts an output phase larger than simulation of the S-MUSE  $f+\dots+10f$  system. First, S-MUSE is a different nonlinear system than MUSE, so subtle qualitative differences may be expected between the models. In particular, simulation of the S-MUSE  $f+2f$  system predicts a slightly larger output phase (not shown) than simulation of the S-MUSE  $f+\dots+10f$  system, which is opposite to what is seen in Fig. 2 predicted by the MUSE model. Therefore, one should not be prejudiced as to whether they expect S-MUSE approximate analytic solutions to predict larger or smaller phase distortions than the S-MUSE  $f+\dots+10f$  system.

Furthermore, one may suspect that since the  $f+2f$  MUSE simulation predicts an output phase very close to the  $f+\dots+10f$  MUSE simulation in Fig. 2, that the linear (drive) mode and a 3IM mode would be sufficient in the analytic expression to approximate the numerical S-MUSE solution in Fig. 8. This would logically follow from the fact that a system that only accounts for second harmonic excitations on the beam can only produce 3IM distortions at the fundamental, and cannot produce 5IM distortions at the fundamental. However, the analytic solution to the  $f+2f$  S-MUSE system contains an infinite number of complex exponential modes [12]. In general, we see no obvious or simple relationship between the number of these analytic complex exponential modes required to adequately approximate a solution, and the number of frequencies included in the model. That is, even though the  $f+2f$  S-MUSE system has only two frequencies, the complete analytic solution to this system has an infinite number of complex exponentials, and there is no *a priori* reason to expect that only two of these exponentials (e.g., the linear and the 3IM modes) are sufficient to approximate the solution. In fact, based on simulations of the  $f+2f$  S-MUSE system (not shown) we find that the analytic solution to the  $f+2f$  S-MUSE system would also require three complex exponential modes (the drive, the 3IM, and one other) to adequately approximate the output phase. (Note that this third analytic mode would not be the same 5IM mode of Fig. 8, because the  $f+2f$  system cannot describe 5th order intermodulation physics.) In any event, in Fig. 8, we see that three complex exponentials, specifically the linear, the 3IM, and the 5IM modes are necessary and sufficient to analytically approximate the S-MUSE  $f+\dots+10f$  system. In turn, we claim that this three-mode analytic solution is a

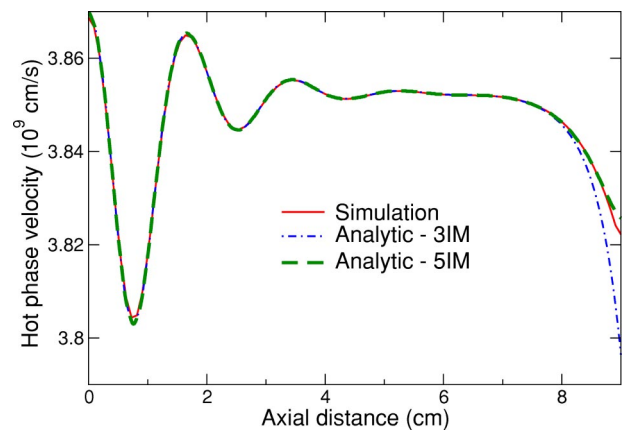


FIG. 9. Analytic and numerical predictions of S-MUSE hot phase velocity at the fundamental frequency. Inclusion of the 3IM and 5IM contributions to the analytic solution, Eq. (6), are required to match the numerical results. All of the complex exponentials from the linear portion of the analytic solution are included to get the correct behavior of the hot phase velocity for  $z < 4$  cm. The numerical solution includes circuit frequencies up to the third harmonic and ten space charge harmonics.

good approximation to the infinite frequency system that is technically needed to represent the partial differential equations S-MUSE was derived from.

For more insight into how the hot phase velocity at the fundamental changes to produce phase distortion, we consider the evolution of the fundamental voltage phase  $\theta_1(z)$  as defined in Eq. (4) and computed from Eq. (6). For simplicity we consider input powers for which only the 3IM contribution to the analytic solution is required to match the numerical solution (e.g.,  $P_{in}$  less than  $-28$  dBm in Fig. 8). For such inputs we have

$$\theta_1(z) = \tan^{-1} \left[ \frac{\text{Im}\{A_{dr}e^{(\mu_{dr}+i\kappa_{dr})z} + A_{nl}e^{(\mu_{nl}+i\kappa_{nl})z}\}}{\text{Re}\{A_{dr}e^{(\mu_{dr}+i\kappa_{dr})z} + A_{nl}e^{(\mu_{nl}+i\kappa_{nl})z}\}} \right]. \quad (8)$$

Working through the calculations in Appendix A one can show that for the input powers under consideration  $|A_{dr}| \gg |A_{nl}|$ . However, for large enough values of  $z$  the terms  $A_{dr}e^{\mu_{dr}z}$  and  $A_{nl}e^{\mu_{nl}z}$  can become comparable since  $\mu_{nl} = 3\mu_{dr}$ . In the limiting cases of small and large  $z$  one has  $d\theta_1/dz = \kappa_{dr}$  and  $d\theta_1/dz = \kappa_{nl}$ , respectively, implying constant values of hot phase velocity via Eq. (5). The limiting case of small  $z$  is seen, for example, between 4 cm and 7 cm in Fig. 7 [the behavior for  $z < 4$  cm is due to the complex exponential modes neglected in Eq. (6)]. Since 3IMs rarely attain comparable power levels to fundamentals before power saturation, the limiting case of large  $z$  where  $d\theta_1/dz = \kappa_{nl}$  is not attained. Therefore the change in hot phase velocity as a function of distance along the TWT for  $z > 7$  cm in Fig. 7 reflects the evolution of the relative weights of the modes in Eqs. (6) and (8).

In Fig. 9 we show S-MUSE numerical solutions and analytic predictions of the evolution of the hot phase velocity for  $P_{in} = -20$  dBm. Consistent with Fig. 8 the contributions from the 3IM and 5IM terms are required for this input power to

accurately model the evolution of the hot phase velocity seen in the numerical solution.

#### IV. AMPLITUDE-PHASE MODEL AND S-MUSE

A popular model for predicting amplifier performance using the nonlinear input-output amplitude and phase transfer characteristics is the so-called amplitude-phase (AP) model [2]. In this section we compare an AP model that uses the analytic solution for the output phase from Eq. (6) to S-MUSE simulations with two frequency inputs. While AP models have been proposed and studied, none have used analytic solutions to nonlinear physics based models for the transfer curves. As in Sec. III, we restrict our attention to input powers in the “linear gain region” of the AM/AM curve.

For an input voltage

$$x(t) = A(t)\cos(\omega_c t), \quad (9)$$

the output voltage in the linear portion of the AM/AM curve for the AP model is

$$y(t) = \gamma A(t)\cos\{\omega_c t + \tilde{\Phi}[A(t)]\}, \quad (10)$$

where  $\gamma$  is a constant gain factor, and  $\tilde{\Phi}(V_{in})$  is the voltage phase difference between the output and input for an input of  $V_{in} \cos \omega_c t$ .  $\tilde{\Phi}(V_{in})$  in Eq. (10) is obtained from  $\Phi(P_{in})$  in Eq. (2) by using [7]

$$P_{in} = \frac{2V_{in}^2}{\tilde{K}}, \quad (11)$$

where  $\tilde{K}$  is the circuit interaction impedance at frequency  $\omega_c$ .

If we choose

$$A(t) = 4V_{in} \cos(\omega_m t), \quad (12)$$

then  $x(t)$  can be equivalently written as

$$x(t) = 2V_{in} \{\cos[(\omega_c + \omega_m)t] + \cos[(\omega_c - \omega_m)t]\} \quad (13)$$

and the output of the AP model is

$$y(t) = \gamma 4V_{in} \cos(\omega_m t)\cos\{\omega_c t + \tilde{\Phi}[4V_{in} \cos(\omega_m t)]\}. \quad (14)$$

Using  $\tilde{\Phi}$  predicted by Eq. (6) we compute the output spectrum of Eq. (14) and compare it to a simulation of the S-MUSE equations where the input is given by Eq. (13). We perform the calculations for two different input powers and two different values of  $\omega_m$  with  $\omega_c/2\pi = 14.0$  GHz.

First we fix the input power to  $-30$  dBm and compute the spectra for  $\omega_m/2\pi = 1.0$  MHz and  $\omega_m/2\pi = 100.0$  MHz. The results for the narrow spacing are shown in Fig. 10 and the results for the wide spacing are shown in Fig. 11. For  $\omega_m/2\pi = 1.0$  MHz the 3IM and 5IM predictions of the AP model are 2.3 dB and 4.2 dB below those of the simulation, respectively. For  $\omega_m/2\pi = 100.0$  MHz the 3IM and 5IM predictions of the AP model are 2.9 dB and 4.7 dB below those of the simulation, respectively. Since  $\tilde{\Phi}$  is computed at a

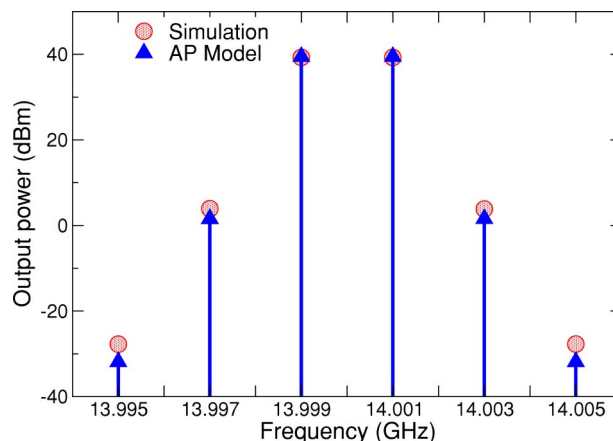


FIG. 10. Comparison of S-MUSE simulation and the AP model output spectra for two input tones. The input power is  $P_{in} = -30$  dBm and the modulation frequency is  $\omega_m/2\pi = 1.0$  MHz.

single frequency, namely  $\omega_c$ , the AP model is expected to apply only over a narrow band of frequencies about  $\omega_c$ . We see that the AP model with a narrow frequency spacing is in closer agreement with the simulation.

For the same frequency spacings we repeated the above calculations with an input power  $P_{in} = -23$  dBm. The results for the narrow spacing are given in Fig. 12 and the results for the wide spacing are given in Fig. 13. In both cases the AP model predictions of the 3IM are about 5 dB lower than the simulation results, whereas the 5IM predictions are greater than the simulation results by about 2 dB.

While the reasons for the increased deviations of the higher power input relative to the lower power input are not entirely understood, we believe that it might lie in the gain compression that the simulation inherently contains and is ignored in our AP model. Relative to  $P_{in} = -50$  dBm an input of  $P_{in} = -30$  dBm corresponds to 0.11 dB of gain compression, whereas an input of  $P_{in} = -23$  dBm corresponds to 0.5 dB of gain compression predicted by S-MUSE simulations (see Fig. 1). To test this hypothesis an AP model accounting for the gain compression could be constructed and tested.

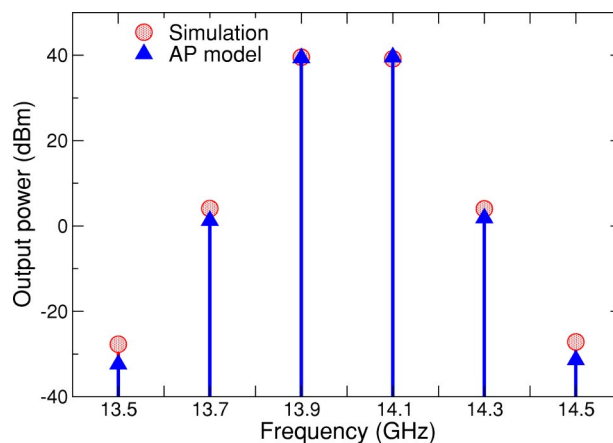


FIG. 11. Comparison of S-MUSE simulation and the AP model output spectra for two input tones. The input power is  $P_{in} = -30$  dBm and the modulation frequency is  $\omega_m/2\pi = 100.0$  MHz.

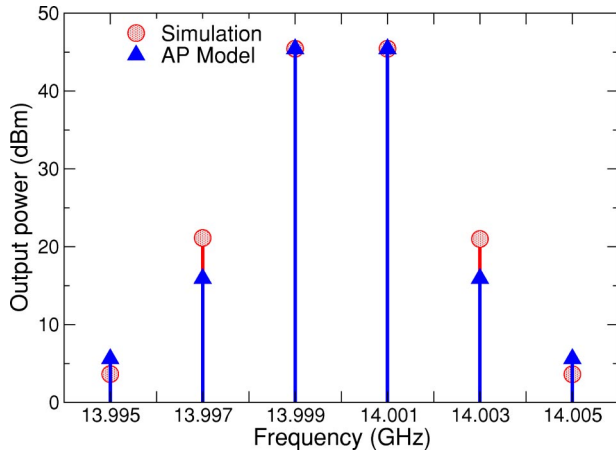


FIG. 12. Comparison of S-MUSE simulation and the AP model output spectra for two input tones. The input power is  $P_{in} = -23$  dBm and the modulation frequency is  $\omega_m/2\pi = 1.0$  MHz.

It is instructive to note that the AP model does not predict spectral content at the harmonics of the carrier frequency  $\omega_c$ , even though it is well known that such spectral distortion exists. This fact is inherent in the construction of the AP model since when transfer curves are measured or simulated, attention is restricted to the TWT behavior at the input and output terminals only at the fundamental frequency. The relation between the transfer curve distortions and the harmonic spectrum is important if one is designing devices such as linearizers based only on TWT transfer curves, where the temptation might be to restrict one's attention to only the fundamental frequency. In the case of phase distortion Sec. III provides what we believe to be the key connections between harmonic distortions and phase distortion at the fundamental.

## V. PARAMETRIC DEPENDENCE OF PHASE DISTORTION

In Sec. III we showed that the second harmonic frequency influences output phase at the fundamental frequency

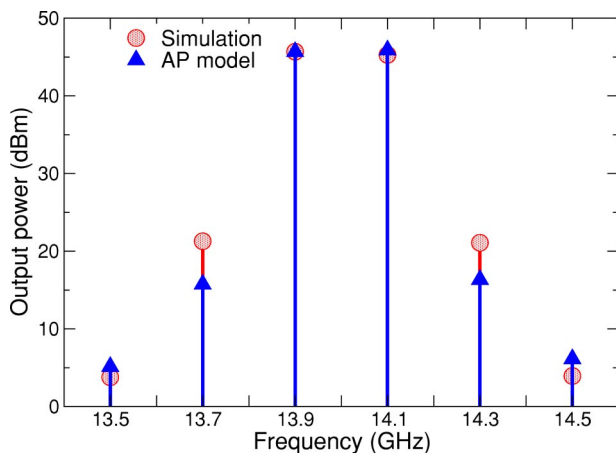


FIG. 13. Comparison of S-MUSE simulation and the AP model output spectra for two input tones. The input power is  $P_{in} = -23$  dBm and the modulation frequency is  $\omega_m/2\pi = 100.0$  MHz.

TABLE III. X-WING TWT electron beam and circuit parameters.

Parameter	Value
Cathode voltage	-2.75 kV
Beam current	0.22 A
Beam radius	0.55 mm
Helix radius	1.4 mm

through an intermodulation process. Therefore, it is of interest to know how phase distortion at the fundamental depends on circuit dispersion and electron beam parameters at the second harmonic. Using LATTE we look at the dependence of the AM/PM distortion at the fundamental on the cold circuit phase velocity  $\tilde{v}_{ph}$ , circuit interaction impedance  $\tilde{K}$ , and electron beam space charge reduction factor  $\tilde{R}$  at the second harmonic. We independently set these parameters to five values and generate AM/AM and AM/PM curves for each parameter value. The values are evenly spaced between the respective parameter value at the fundamental and the parameter value at the third harmonic. The parameter values chosen are not necessarily physically realizable since we are directly changing the parameter, not the circuit dimensions or electron beam dimensions to attain the set of parameters. However, the results give a good indication of the relative role the parameters play in phase distortion.

We expect the phase distortion to behave differently when the second harmonic is in the linear gain bandwidth of the TWT, since the second harmonic will then have a larger amplitude and produce a larger fundamental intermodulation. Therefore we choose two TWT designs for this study, one in which the second harmonic is in the linear gain bandwidth, and one in which the second harmonic is out of the linear gain bandwidth. For the “narrow band” TWT we use the Ku-band design of Sec. III, and for the “wide band” design we use simulation parameters based on the experimental Wisconsin Northrup Grumman (X-WING) 1.5 octave C-band TWT [19]. The electron beam and circuit parameters for X-WING are listed in Table III and the relevant dispersion parameters for X-WING are listed in Table IV.

In Figs. 14–16 we show the simulation results for the Ku-band TWT. From Fig. 14 we see that the phase distortion is relatively unaffected by the phase velocity at the second harmonic. We see from Fig. 15 that the interaction impedance at the second harmonic can affect the input power at which the maximum AM/PM conversion occurs and the maximum value of AM/PM conversion. Furthermore, larger values of interaction impedance can produce AM/PM con-

TABLE IV. X-WING TWT dispersion parameters.

$f$ (GHz)	$\tilde{v}_{ph}(\times 10^9$ cm/s)	$\tilde{K}(\Omega)$	$\tilde{R}$
2.00	2.487	103.094	$2.787 \times 10^{-2}$
4.00	2.515	38.132	$9.802 \times 10^{-2}$
6.00	2.552	15.411	$1.846 \times 10^{-1}$

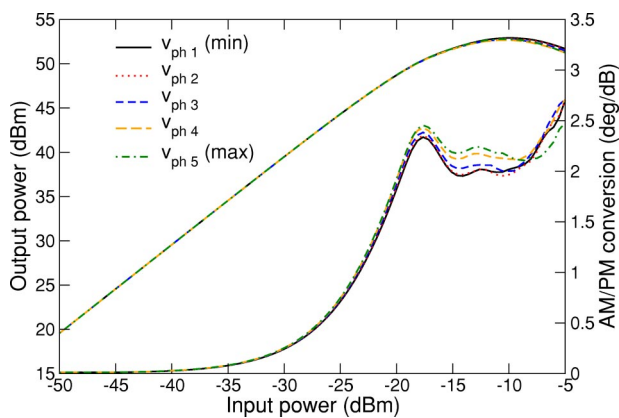


FIG. 14. AM/AM and AM/PM distortion for the Ku-band design at 14 GHz for five values of cold circuit phase velocity at the second harmonic. The legend represents the five values ranging from the minimum parameter value (min) to the maximum parameter value (max).

version coefficients of zero. Finally, from Fig. 16 we see that smaller values of space charge reduction factor have a larger maximum AM/PM conversion coefficient, but the input power where the maximum AM/PM conversion is attained is unchanged.

In Figs. 17–19 we show the simulation results for the C-band TWT. From Fig. 17 we see that the phase distortion is relatively unaffected by the phase velocity at the second harmonic as was the case for the narrow band TWT. The interaction impedance at the second harmonic for the wide band TWT displays the clearest trend and has the greatest effect on AM/PM distortion as seen in Fig. 18. Larger values of interaction impedance produce the largest AM/PM distortion. Finally, from Fig. 19 we see that the space charge reduction factor does not have much effect on either the location or value of the maximum AM/PM coefficient.

We expect that analysis of the S-MUSE equations together with additional simulations could be used to understand the relative roles of circuit and beam harmonics on

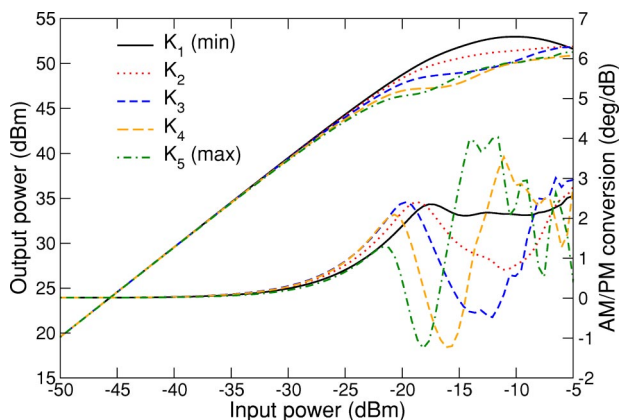


FIG. 15. AM/AM and AM/PM distortion for the Ku-band design at 14 GHz for five values of cold circuit interaction impedance at the second harmonic. The legend represents the five values ranging from the minimum parameter value (min) to the maximum parameter value (max).

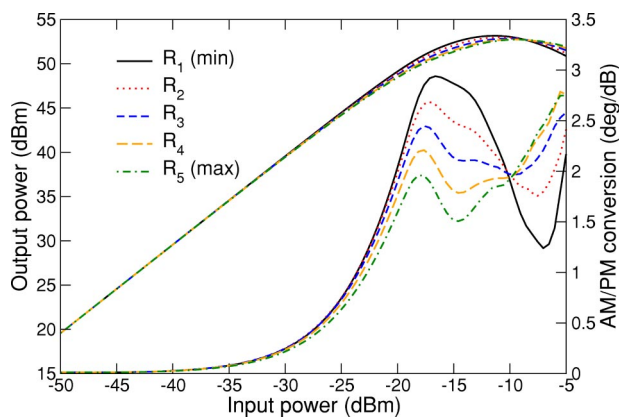


FIG. 16. AM/AM and AM/PM distortion for the Ku-band design at 14 GHz for five values of space charge reduction factor at the second harmonic. The legend represents the five values ranging from the minimum parameter value (min) to the maximum parameter value (max).

phase distortion, as well as how TWT bandwidth influences phase distortion. However, preliminary investigation has established that such a study will be nontrivial and beyond the scope of this paper. Therefore, we leave the study to future work.

## VI. INSIGHTS INTO TWT LINEARIZATION

In this section we use our insights into the mechanisms of phase distortion to discuss two separate, but related, methods of TWT linearization. TWT linearization is presently a very popular area of research due to the large economic benefits to be gained from high power linear amplification [20].

### A. Phase linearization by harmonic injection

The method of harmonic injection has long been used to reduce the harmonic power in the TWT output (see e.g., Ref. [21]). We have recently reported a theory of harmonic injection

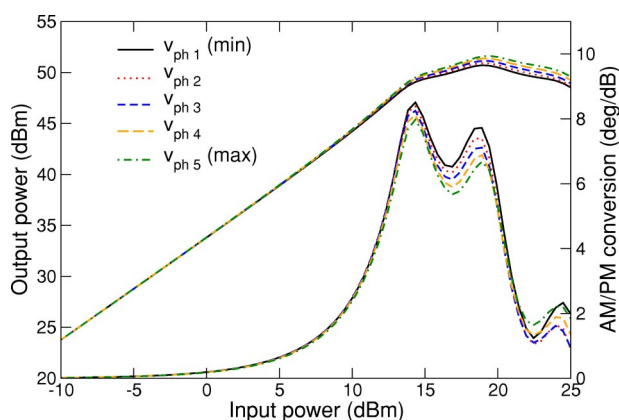


FIG. 17. AM/AM and AM/PM distortion for the C-band design at 2 GHz for five values of cold circuit phase velocity at the second harmonic. The legend represents the five values ranging from the minimum parameter value (min) to the maximum parameter value (max).

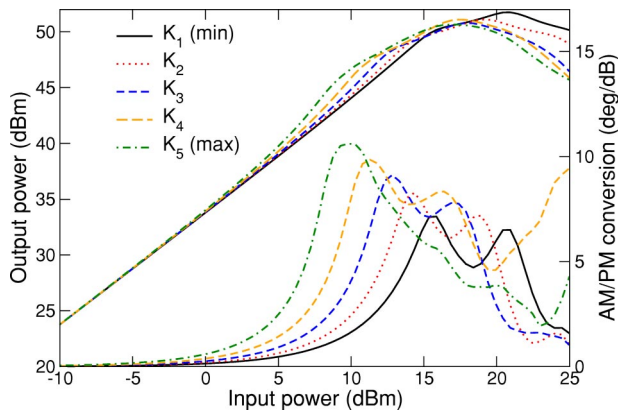


FIG. 18. AM/AM and AM/PM distortion for the C-band design at 2 GHz for five values of cold circuit interaction impedance at the second harmonic. The legend represents the five values ranging from the minimum parameter value (min) to the maximum parameter value (max).

tion based on the models used in this paper [11,12,22]. The harmonic injection theory describes the fundamental and harmonic waves as superpositions of driven and nonlinear modes. This is similar to what is described in Sec. III B, but in the case of harmonic injection the dominant *nonlinear* contribution at the fundamental and harmonic is due to a second order product rather than a third order product.

In standard harmonic injection schemes the inputs are adjusted such that the modes of the harmonic solution cancel at the output, and hence the amount of harmonic in the output wave form is reduced. However, if the claims that we have made in this paper are true, i.e., that the voltage at the fundamental should be considered as a superposition of modes, then one should also be able to use harmonic injection to manipulate the voltage phase at the fundamental by manipulating the relative magnitudes and phases of the modes. In Figs. 20 and 21 we demonstrate using the large signal code LATTE that this is indeed possible.

We consider harmonic injection in the X-WING TWT (see Sec. V) with a fundamental frequency of 2 GHz. In Fig.

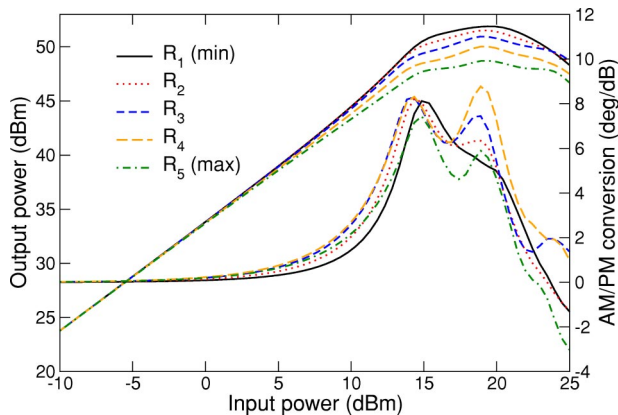


FIG. 19. AM/AM and AM/PM distortion for the C-band design at 2 GHz for five values of space charge reduction factor at the second harmonic. The legend represents the five values ranging from the minimum parameter value (min) to the maximum parameter value (max).

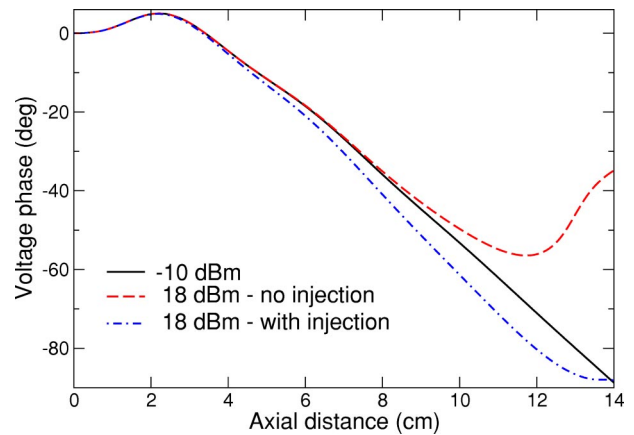


FIG. 20. Circuit voltage phase vs axial distance for a small signal input ( $-10$  dBm), a large signal input (18 dBm), and the large signal input with harmonic injection. With harmonic injection the output phase for the large signal input is made equal to the output phase for the small signal input. The injected harmonic power and phase are 17 dBm and  $-47.5^\circ$ , respectively. The fundamental input phase is  $0^\circ$  in all cases. Voltage phase is with respect to the cold circuit wave at 2 GHz.

20 we show the relative circuit voltage phase at the fundamental frequency vs axial distance for a “small signal” input ( $-10$  dBm), a large signal input (18 dBm) without harmonic injection, and the large signal input with harmonic injection. Indeed one sees that with harmonic injection the fundamental output phase may be made to be same value as the small signal output phase, even with a large signal input. In Fig. 21 we show the fundamental and harmonic circuit powers vs axial distance with and without the harmonic injection. This shows first that 18 dBm input is a large signal input since the fundamental circuit power is saturating at the output, and second that to obtain this “phase linearization” the fundamental output power is reduced by about 3 dB.

It is important to note that the large signal LATTE model

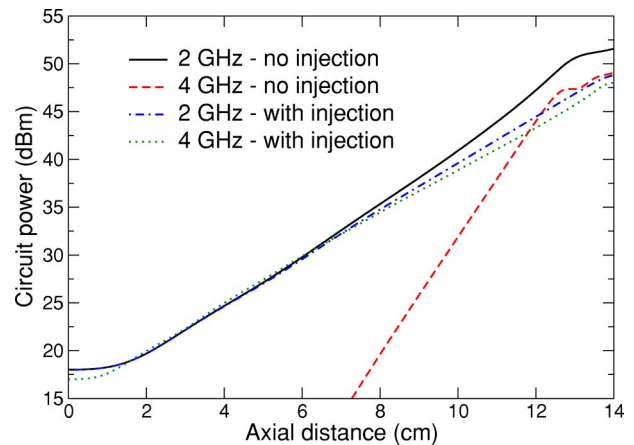


FIG. 21. Circuit power vs axial distance for a large signal input (18 dBm) with and without harmonic injection to obtain “phase linearization.” The fundamental output power with harmonic injection is reduced by about 3 dB from the case with no injection. The injected harmonic power and phase are 17 dBm and  $-47.5^\circ$ , respectively. The fundamental input phase is  $0^\circ$  in both cases.

has *no* representation of the distinct modes in its formulation, but Figs. 20 and 21 demonstrate that the modes do exist in the solutions to LATTE (also see Refs. [10,12,22] for further proof of this fact).

**B. The linearization method of Chen *et al.***

Chen *et al.* [23] have recently presented a new method of linearizing TWTs. The method involves applying small bias voltages to the (electrically floating) helix based on either “direct feed” or feedback processing of the input signal. The bias voltage is a function of the input power “envelope,” and has the effect of adjusting the electron beam velocity by changing the potential an electron sees as it enters the helix. The change in electron beam velocity can be equivalently viewed as a change in electron beam voltage. The explanation for how the linearization technique works offered in Ref. [23] is based on the view that phase distortion is due to slowing down of electrons in the beam. Our view of phase distortion led us to hypothesize an alternative explanation, consistent with the conceptual framework described here and in Ref. [12]. The experimental results given in Figs. 4 and 5 of Ref. [23] are for TWT input conditions 9 dB backed off from saturation, well within the range of applicability of our theory.

We submit that linearization using the technique of Ref. [23] of a two tone input signal as shown in Figs. 4 and 5 of Ref. [23], and similar to the input spectra of Sec. IV of this paper, should not be explained in terms of phase distortion. First, we claim that a constant voltage applied to the helix to compensate for phase distortion for single frequency sine wave inputs can be explained in terms of linear TWT theory. Second, we claim that the linearization of a two tone input signal with the technique should be viewed as the injection of a beam velocity modulation at the difference frequency of the two input frequencies.

Applying a dc voltage bias to the helix compensates for the nonlinear output phase distortion by changing the electrical length of the TWT, i.e., the number of wavelengths in the TWT, based on the *linear* Pierce theory [14]. That is, the dependence of the linear “hot wave number”  $\beta_{lin}$  (see Sec. III) on input voltage is sensitive enough such that a small change in beam voltage can account for a non-negligible phase change at the output of the TWT. Using the driven term of Eq. (6) one gets

$$\beta_{lin} = \kappa_{dr}(V_0) + f_1 \omega_0 \sqrt{\frac{m_e}{2eV_0}}, \quad (15)$$

where  $V_0$  is beam voltage,  $m_e$  is electron mass, and  $e$  is electron charge. In Eq. (15)  $\kappa_{dr}(V_0)$  is the imaginary part of the eigenvalue of  $\mathbf{A}_1$  (see Appendix A) corresponding to the exponentially growing solution, and we have used that  $eV_0 = (1/2)m_e u_0^2$ . One can show that for small changes in  $V_0$  Eq. (15) is approximately a linear function of  $V_0$  and that the accumulated phase  $\beta_{lin}(V_0)L$  can change by as much as  $25^\circ$  for less than a 1% change in  $V_0$ .

In Fig. 22 we show LATTE calculations of output phase vs input power for five values of beam voltage. The total range of beam voltages spans less than 1% of the design

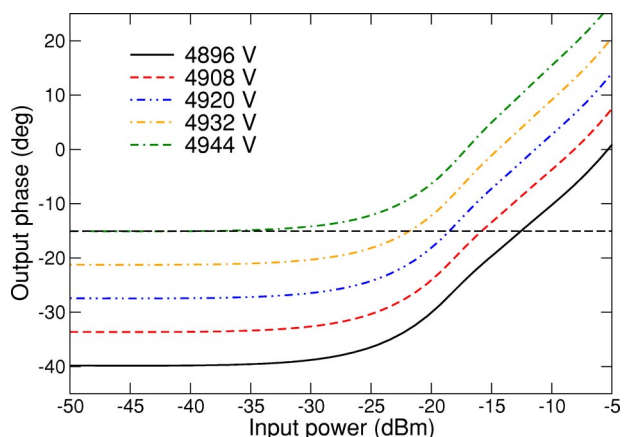


FIG. 22. Output phase vs input power for several values of dc beam voltage for the Ku-band TWT design. The range of the bias voltages spans 48 V, less than 1% of the design beam voltage.

beam voltage, but the phase difference between these values, which to leading order can be predicted by linear theory, is about  $25^\circ$ . To obtain a constant output phase for any value of input power, one can select from the parametrized output phase vs input power curves. One chooses the curve that passes through the desired value of output phase and input power, and sets the bias voltage, by a feedback loop, for example, such that the beam voltage is equal to the value labeling the intersecting curve. In this manner the phase distortion, which is a single frequency input measurement, can be compensated for. Note that the input power used for the experiment in Ref. [23] would correspond approximately to  $P_{in} = -26$  dBm in Fig. 22, i.e., 9 dB backed off from saturation (see Fig. 1). To show that the phase offset for different helix voltages is well approximated by linear theory for all input powers, we include input powers up to and beyond saturation.

We saw in Sec. IV that an input signal consisting of two frequencies with a spacing of  $2\omega_m$  centered about  $\omega_c$  could be written as

$$x(t) = \cos(\omega_m t) \cos(\omega_c t), \quad (16)$$

where typically  $\omega_m \ll \omega_c$ . If such a signal is passed through a diode for envelope detection, the diode output signal will have a frequency of  $2\omega_m$  due to the diode rectification. If this low frequency signal is then used for the helix bias, one effectively has an input modulation on the electron beam voltage at the difference frequency  $2\omega_m$ . Furthermore, this signal is applied to a “grid compensation circuit” in Ref. [23] which would also have the effect of an input modulation on the electron beam voltage at the difference frequency  $2\omega_m$ . Therefore, we claim that the new technique of linearization put forward by Chen *et al.* [23] is equivalent to injecting a difference frequency modulation on the beam velocity.

Our recent theory of harmonic injection in a TWT [11,12] has shown that it is theoretically possible to obtain intermodulation cancellation by injection of the difference frequency in the circuit voltage. However, because the difference frequency is typically outside of the linear gain bandwidth, substantial input powers at the difference fre-

quency are expected to be required. Since the electron beam has no such bandwidth limitations, it is expected that modest difference frequency modulations of the beam velocity, such as with the proposed scheme, may be more effective than difference frequency injection of circuit voltage. This topic will be explored further in a future work.

## VII. CONCLUSIONS

Phase distortion has been said to “dominate TWT nonlinearity” [23] in TWTs. In the literature many authors have attributed phase distortion to the slowing down of electrons in the electron beam, i.e., the reduction of the average electron beam velocity (see, e.g., Refs. [4,5,23]). Through simulation and analysis we offer evidence that phase distortion, at least prior to 1 dB gain compression, is not due to slowing down of electrons in the beam. Rather, we show that *phase distortion arises from harmonic generation in the electron beam and an intermodulation process that results in distortions at the fundamental*.

The implications of the understanding of phase distortion are many. First, provided with a view of nonlinear TWT physics, one may be led to consider alternative parametric dependencies and explanations for physical phenomenon. We have provided examples of such studies in Secs. IV–VI. Furthermore, the understanding may possibly lead to improved TWT designs, since the notions that a designer has about how a device works inevitably influence how they proceed with a design.

Using the MUSE, S-MUSE, and LATTE TWT models we explore phase distortion in a TWT. The unique ability of the MUSE model to systematically suppress the effects of different frequencies in the nonlinear TWT behavior shows that the second harmonic distortion in the electron beam is the dominant factor in causing phase distortion, at least prior to gain compression. Furthermore, we show that the average slowing down of electrons is not the primary cause of phase distortion using MUSE simulations in addition to large signal LATTE simulations that were corrected to remove the average velocity reduction.

With the approximate analytic solution to the S-MUSE model we give an insightful picture of the fundamental frequency also being a self-intermodulation product. We show that prior to 1 dB gain compression the analytic solution accounting for the 3IM and 5IM contributions has a phase distortion that closely matches the phase distortion from simulation of the S-MUSE equations. We also show that the change in voltage hot phase velocity which causes phase distortion is due to an evolving balance of the driven and intermodulation modes in the solution.

Leveraging off of our understanding of phase distortion we consider several applications. First, we compare S-MUSE simulations to an amplitude-phase model that uses the approximate analytic solution to S-MUSE for the output phase vs input power. We see that there are discrepancies in the intermodulation spectra predicted by the two methods, and that the disagreement is worse for wider frequency spacings and for larger input powers. The study reinforces our view that the amplitude-phase model is an incomplete picture of

nonlinear TWT physics, and that measuring single frequency phase distortion characteristics captures only a part of the harmonic and intermodulation physics happening internal to the TWT. Second, we study how phase distortion depends on circuit and electron beam parameters at the second harmonic. We find that circuit interaction impedance at the second harmonic has the greatest effect on AM/PM distortion, especially when the second harmonic is within the linear gain bandwidth of the TWT. Third, we use the insight that the fundamental is composed of driven and nonlinear modes, together with knowledge of the mechanisms of harmonic injection [11,12,22], to propose harmonic injection as a method of phase linearization. We show using the large signal code LATTE that with a properly adjusted harmonic input, one can obtain the same fundamental output phase for small and large signal fundamental inputs. Note that earlier explanations for phase distortion, such as that of Ref. [6], do not easily explain this phenomenon because they do not account for the existence of driven and nonlinear modes. Finally, we consider a technique of linearization [23] and offer a physical explanation for the linearization mechanism. In this case again we propose that phase distortion is not the proper way of looking at the linearization, and that a view of the intermodulation and difference frequency physics is required.

## ACKNOWLEDGMENTS

The authors gratefully acknowledge support in part by AFOSR Grant No. 49620-00-1-0088 and by DUSD (S&T) under the Innovative Microwave Vacuum Electronics Multidisciplinary University Research Initiative (MURI) program, managed by the United States Air Force Office of Scientific Research under Grant No. F49620-99-1-0297. We would like to thank Carter Armstrong, Tom Hargreaves, and Aarti Singh for their useful suggestions on the manuscript.

## APPENDIX A: ANALYTIC FORMULAS FOR EQ. (6)

In this appendix we provide a formalism for solving the S-MUSE model for the components necessary to compute Eq. (6). We use the vector notation of Ref. [7] where  $\mathbf{x}_\ell = [\mathbf{x}_{\ell_1} \cdots \mathbf{x}_{\ell_s}]^T = [\tilde{V}_\ell \tilde{I}_\ell \tilde{E}_\ell \tilde{v}_\ell \tilde{\rho}_\ell]^T$ . The differential equation for  $\mathbf{x}_\ell$  is

$$\dot{\mathbf{x}}_\ell = \mathbf{A}_\ell \mathbf{x}_\ell + \sum_{\substack{m,n \\ f_m + f_n = f_\ell}} \mathbf{H}_{\ell mn}(\mathbf{x}_m, \mathbf{x}_n), \quad (\text{A1})$$

where matrix and tensor components  $\mathbf{A}_{\ell_{ij}}$  and  $\mathbf{H}_{\ell_{m_j n_k}}$  are listed in Appendix II of Ref. [7]. One can show that Eq. (A1) may be solved with a series solution

$$\mathbf{x}_\ell = \sum_{\alpha=1}^{\infty} \mathbf{x}_\ell^{(\alpha)}, \quad (\text{A2})$$

and that this series converges under the appropriate conditions [10,12]. The index  $\alpha$  is related to the order of intermodulation product [10]. The formulas for the terms of the series are given by

$$\mathbf{x}_\ell^{(1)} = e^{\mathbf{A}_\ell z} \mathbf{w}_\ell, \quad \alpha = 1, \quad (\text{A3})$$

$$\mathbf{x}_\ell^{(\alpha)} = \int_0^z e^{\mathbf{A}_\ell(z-\tau)} \sum_{\beta=1}^{\alpha-1} \sum_{m,n} \mathbf{H}_{\ell mn}[\mathbf{x}_m^{(\beta)}(\tau), \mathbf{x}_n^{(\alpha-\beta)}(\tau)] d\tau, \quad f_m + f_n = f_\ell$$

$$\alpha \geq 2, \quad (\text{A4})$$

where  $\mathbf{w}_\ell$  contains the initial values for frequency  $f_\ell \omega_0$  [7] and  $e^{\mathbf{A}_\ell z}$  is the matrix exponential of the matrix  $\mathbf{A}_\ell z$  [24].

The complex exponential modes of the vector  $\mathbf{x}_\ell^{(\alpha)}$  are indexed by  $p$

$$\mathbf{x}_\ell^{(\alpha)}(z) = \sum_{p=1}^{N_\ell^{(\alpha)}} \mathbf{a}_\ell^{(\alpha)[p]} e^{(\mu_\ell^{(\alpha)[p]} + i\kappa_\ell^{(\alpha)[p]})z}, \quad (\text{A5})$$

with  $\mathbf{a}_\ell^{(\alpha)[p]}$  a complex vector. Sums like Eq. (A5) are ordered so that  $\mu_\ell^{(\alpha)[1]}$  is the largest of all the  $\mu_\ell^{(\alpha)[p]}$ .

For brevity we only provide details to compute the 3IM contribution to Eq. (6) and refer the reader to Refs. [11,12] for details on how to compute higher order contributions. To compute the terms of Eq. (6) and the input-output phase difference  $\Phi$  we need to compute in order the  $p=1$  modes  $\mathbf{x}_1^{(1)[1]}$ ,  $\mathbf{x}_2^{(2)[1]}$ ,  $\mathbf{x}_1^{(3)[1]}$ . Details of the calculations are provided in Ref. [12].

### 1. Series term $\mathbf{x}_1^{(1)}$

The dominant term in the first order ( $\alpha=1$ ) drive frequency ( $\ell=1$ ) solution is

$$\mathbf{x}_1^{(1)[1]} = \mathbf{a}_1^{(1)[1]} e^{\mu_1^{(1)[1]} z} e^{i\kappa_1^{(1)[1]} z}, \quad (\text{A6})$$

where

$$\mathbf{a}_1^{(1)[1]} = \mathbf{P}_1 \mathbf{Q} \mathbf{P}_1^{-1} \mathbf{w}_1, \quad (\text{A7})$$

$$\mu_1^{(1)[1]} = \text{Re}\{\lambda_{1,1}\}, \quad (\text{A8})$$

$$\kappa_1^{(1)[1]} = \text{Im}\{\lambda_{1,1}\}, \quad (\text{A9})$$

and

$$\mathbf{Q}_{i,j} = \begin{cases} 1, & i = j = 1 \\ 0, & \text{otherwise,} \end{cases} \quad (\text{A10})$$

assuming that  $\mathbf{P}_1$ , the modal matrix of  $\mathbf{A}_1$ , has the eigenvector associated with  $\lambda_{1,1}$ , the eigenvalue of  $\mathbf{A}_1$  with the largest real part, in its first column. Then for Eq. (6) we have

$$\mathbf{A}_{\text{dr}} = \mathbf{a}_1^{(1)[1]}, \quad (\text{A11})$$

$$\mu_{\text{dr}} = \mu_1^{(1)[1]}, \quad (\text{A12})$$

$$\kappa_{\text{dr}} = \kappa_1^{(1)[1]}. \quad (\text{A13})$$

### 2. Series term $\mathbf{x}_2^{(2)}$

For  $\mathbf{x}_2^{(2)[1]}$  we have

$$\mathbf{x}_2^{(2)[1]} = \text{dominant mode of} \left\{ \int_0^z e^{\mathbf{A}_2(z-\tau)} \times \mathbf{H}_{211}[\mathbf{x}_1^{(1)[1]}(\tau), \mathbf{x}_1^{(1)[1]}(\tau)] d\tau \right\}. \quad (\text{A14})$$

Let

$$\mathbf{c}_2 = \mathbf{H}_{211}(\mathbf{a}_1^{(1)[1]}, \mathbf{a}_1^{(1)[1]}), \quad (\text{A15})$$

then

$$\mathbf{x}_2^{(2)[1]} = \mathbf{P}_2 \mathbf{S}_2(2\lambda_{1,1}) \mathbf{P}_2^{-1} \mathbf{c}_2 e^{2\lambda_{1,1} z} \quad (\text{A16})$$

$$= \mathbf{a}_2^{(2)[1]} e^{2\mu_1^{(1)[1]} z} e^{i2\kappa_1^{(1)[1]} z}, \quad (\text{A17})$$

where

$$\mathbf{S}_{\ell_{i,j}}(\gamma) \equiv \begin{cases} \frac{1}{\gamma - \lambda_{\ell_j}}, & i = j \\ 0, & \text{otherwise.} \end{cases} \quad (\text{A18})$$

The eigenvalues  $\lambda_{\ell_j}$  of  $\mathbf{A}_\ell$  have the same order as the eigenvectors of  $\mathbf{A}_\ell$  appearing in columns of  $\mathbf{P}_\ell$ . We have assumed that the real part of  $2\lambda_{1,1}$  is larger than the real part of  $\lambda_{2,1}$ , the eigenvalue of  $\mathbf{A}_2$  with the largest real part, and that  $2\lambda_{1,1} \neq \lambda_{2,j}$  for  $j=1, \dots, 5$ , as is most often the case.

### 3. Series term $\mathbf{x}_1^{(3)}$

The third order term at the drive frequency is

$$\mathbf{x}_1^{(3)[1]} = \text{dominant mode of} \left\{ \int_0^z e^{\mathbf{A}_1(z-\tau)} \times [\mathbf{H}_{1,2,-1}(\mathbf{x}_2^{(2)[1]}(\tau), \mathbf{x}_1^{(1)[1]}(\tau)) + \mathbf{H}_{1,-1,2}(\mathbf{x}_1^{(1)[1]}(\tau), \mathbf{x}_2^{(2)[1]}(\tau))] d\tau \right\}. \quad (\text{A19})$$

Let

$$\mathbf{c}_1 = \mathbf{H}_{1,2,-1}(\mathbf{a}_2^{(2)[1]}, \mathbf{a}_1^{(1)[1]}) + \mathbf{H}_{1,-1,2}(\mathbf{a}_1^{(1)[1]}, \mathbf{a}_2^{(2)[1]}), \quad (\text{A20})$$

with  $\mathbf{a}_{-1} = \mathbf{a}_1^*$  then

$$\mathbf{x}_1^{(3)[1]} = \mathbf{P}_1 \mathbf{S}_1(2\lambda_{1,1} + \lambda_{1,1}^*) \mathbf{P}_1^{-1} \mathbf{c}_1 e^{(2\lambda_{1,1} + \lambda_{1,1}^*)z} \quad (\text{A21})$$

$$= \mathbf{a}_1^{(3)[1]} e^{3\mu_1^{(1)[1]} z} e^{i\kappa_1^{(1)[1]} z}. \quad (\text{A22})$$

Therefore for Eq. (6)

$$\mathbf{A}_{\text{nl}} = \mathbf{a}_1^{(3)[1]}, \quad (\text{A23})$$

$$\mu_{\text{nl}} = 3\mu_1^{(1)[1]}, \quad (\text{A24})$$

$$\kappa_{\text{nl}} = \kappa_1^{(1)[1]}. \quad (\text{A25})$$

Any of the TWT state variables may be computed by choosing the appropriate vector components from  $\mathbf{a}_1^{(1)[1]}$  and  $\mathbf{a}_1^{(3)[1]}$ .

Similarly to compute the 5IM contribution to Eq. (6) one needs to compute  $\alpha=4$  and  $\alpha=5$  terms. For details of the computations we refer the reader to Ref. [12].

## APPENDIX B: EFFECT OF AVERAGE BEAM VELOCITY IN LATTE

In this appendix we provide the theory necessary to remove the effect of the reduction of the average beam velocity in the large signal code LATTE. We first need an expression to compute the average velocity from a LATTE simulation, then a way to remove this effect from a subsequent simulation.

In Eulerian coordinates the electron beam average velocity is

$$\langle v(z) \rangle_0 = \frac{1}{2\pi} \int_{2\pi} v^E(z, \psi) d\psi, \quad (\text{B1})$$

which in Lagrangian coordinates becomes [7]

$$\langle v(z) \rangle_0 = \frac{1}{2\pi} \int_{2\pi} v^L(z, \psi_0) \left| \frac{\partial \Psi}{\partial \psi_0} \right| d\psi_0 \quad (\text{B2})$$

$$= \frac{1}{2\pi} \int_{2\pi} \frac{I_0(\psi_0)}{A \rho^L(z, \psi_0)} d\psi_0, \quad (\text{B3})$$

where  $\psi = \omega_0(z/u_0 - t)$  is a phase variable,  $I_0(\psi_0)$  is the dc beam current,  $A$  is the beam cross sectional area, and the other quantities are defined in Sec. II of the paper. We can write  $\rho^L$  using the Fourier synthesis equation in Lagrangian coordinates

$$\rho^L(z, \psi_0) = \sum_{\ell=-\infty}^{\infty} \tilde{\rho}_\ell e^{if_\ell \Psi(z, \psi_0)} \quad (\text{B4})$$

where

$$\tilde{\rho}_\ell = \frac{1}{2\pi} \int_{2\pi} \frac{I_0(\psi_0)}{A v(z, \psi_0)} e^{-if_\ell \Psi(z, \psi_0)} d\psi_0. \quad (\text{B5})$$

For computations the integrals become sums over  $N$  “disks,” we consider a finite number of positive frequencies  $M$ , and we can combine Eqs. (B3)–(B5) to get

$$\langle v(z) \rangle_0 = \sum_{i=1}^N \left[ \sum_{\ell=-M}^M \sum_{j=1}^N \frac{e^{if_\ell(\Psi_i - \Psi_j)}}{v_j} \right]^{-1}, \quad (\text{B6})$$

where we have assumed  $I_0(\psi_0) = I_0$  and used the notation  $\Psi(z, \psi_{0i}) = \Psi_i$  and  $v(z, \psi_{0i}) = v_i$ , where  $\psi_{0i}$  is an initial disk phase. For a simulation with small enough input power we can confirm that Eq. (B6) is correct by comparing it to the average electron beam velocity  $\tilde{v}_0(z)$  computed by the MUSE model.

To remove the effect of  $\langle v(z) \rangle_0$  in a subsequent LATTE simulation, we first compute the adjusted disk velocities

$$\tilde{v}_i = v_i - \langle v \rangle_0 + u_0. \quad (\text{B7})$$

We confirm by computing Eq. (B6) using the adjusted velocities that for the power levels we are interested in we have

$$\langle \tilde{v}_i \rangle_0 = u_0, \quad (\text{B8})$$

then given the adjusted velocities we compute disk phase trajectories  $\tilde{\Psi}_i$  using [7]

$$\frac{\partial \tilde{\Psi}_i}{\partial z} = \frac{\omega_0}{u_0} \left( 1 - \frac{u_0}{\tilde{v}_i} \right). \quad (\text{B9})$$

From the adjusted velocities and phase trajectories we can compute the adjusted electron beam density coefficient given by Eq. (B5) where the integral is replaced by a sum over disks. Finally, one can compute a circuit voltage at the fundamental frequency corresponding to the adjusted beam charge density from the LATTE lossless circuit equations [7]

$$\frac{d\tilde{V}_\ell}{dz} = -\frac{if_\ell \omega_0}{u_0} \tilde{V}_\ell - \frac{if_\ell \omega_0 \tilde{K}_\ell}{\tilde{v}_{\text{ph}\ell}} \tilde{I}_\ell, \quad (\text{B10})$$

$$\frac{d\tilde{I}_\ell}{dz} = -\frac{if_\ell \omega_0}{\tilde{K}_\ell \tilde{v}_{\text{ph}\ell}} \tilde{V}_\ell - \frac{if_\ell \omega_0}{u_0} \tilde{I}_\ell + if_\ell \omega_0 A \tilde{\rho}_\ell, \quad (\text{B11})$$

where  $\tilde{V}_\ell$  and  $\tilde{I}_\ell$  are the complex circuit voltage and circuit current envelopes as defined in Eq. (1),  $\tilde{K}_\ell$  is the circuit interaction impedance at frequency  $f_\ell \omega_0$ ,  $\tilde{v}_{\text{ph}\ell}$  is the circuit phase velocity at frequency  $f_\ell \omega_0$ , and  $A$  is the electron beam cross sectional area.

- 
- [1] A. Berman and C. Mahle, IEEE Trans. Commun. Technol. **18**, 37 (1970).  
 [2] A. Saleh, IEEE Trans. Commun. **COM-29**, 1715 (1981).  
 [3] R. Carter, W. Bösch, V. Srivastava, and G. Gatti, IEEE Trans. Electron Devices **48**, 178 (2001).  
 [4] A. Gilmour, Jr., *Principles of Traveling Wave Tubes* (Artech House, Boston, 1994).  
 [5] E. Ezura and T. Kano, IEEE Trans. Electron Devices **ED-22**,

- 890 (1975).  
 [6] G. Dimonte and J. Malmberg, Phys. Fluids **21**, 1188 (1978).  
 [7] J. Wöhlbier, J. Booske, and I. Dobson, IEEE Trans. Plasma Sci. **30**, 1063 (2002).  
 [8] The code LATTE/MUSE Numerical Suite solves the three models for arbitrary TWT geometries. The code and the input files that generated the results in this paper are available at <http://www.lmsuite.org>

- [9] X. Li, J. Wöhlbier, S. Jin, and J. Booske, Phys. Rev. E (to be published).
- [10] J. Wöhlbier, I. Dobson, and J. Booske, Phys. Rev. E **66**, 56504 (2002).
- [11] J. Wöhlbier, J. Booske, and I. Dobson, IEEE Trans. Plasma Sci. (to be published).
- [12] J. Wöhlbier, Ph.D. thesis, University of Wisconsin–Madison, 2003.
- [13] The “stream wave” is a hypothetical wave of frequency  $\omega_0$  traveling with speed  $u_0$ .
- [14] J. Pierce, *Traveling Wave Tubes* (Van Nostrand, Princeton, NJ, 1950).
- [15] T. Antonsen, Jr., and B. Levush, IEEE Trans. Plasma Sci. **26**, 774 (1998).
- [16] We estimate a constant value of 0.2 % reduction, which is the maximum reduction achieved, over half of the entire length for which the reduction takes place.
- [17] We define a  $K$ th order intermodulation product of frequencies  $f_1, f_2, \dots, f_P$  as  $r_1 f_1 + r_2 f_2 + \dots + r_P f_P$  where  $r_j$  are integers (possibly zero) and  $K = |r_1| + |r_2| + \dots + |r_P|$ . This structure includes fundamental and harmonic frequencies if all but one of the  $r_j$  are zero.
- [18] By “large signal phase distortion” we mean predictions of the phase distortion by the large signal code LATTE.
- [19] M. Wirth, A. Singh, J. Scharer, and J. Booske, IEEE Trans. Electron Devices **49**, 1082 (2002).
- [20] D. Komm, R. Benton, H. Limburg, W. Menninger, and X. Zhai, in *International Vacuum Electronics Conference* (IEEE, Piscataway, NJ, 2000).
- [21] J. Hamilton and D. Zavadil, Microwave J. **15**, 24 (1972).
- [22] A. Singh, J. Wöhlbier, J. H. Booske, and J. E. Scharer, Phys. Rev. Lett. **92**, 205005 (2004).
- [23] T. Chen, Y. Goren, C. Jensen, P. Lally, and D. Gagne, *2002 IEEE-MTT-S International Microwave Symposium Digest* (IEEE, Piscataway, NJ, 2002), Vol. 2, pp. 773–776.
- [24] E. Coddington and N. Levinson, *Theory of Ordinary Differential Equations* (McGraw-Hill, New York, 1955).